A&A 373, 932–949 (2001)
DOI: 10.1051/0004-6361:20010535


Astronomy & Astrophysics

# The highly collimated bipolar outflow of OH 231.8+4.2⋆

J. Alcolea[1], V. Bujarrabal[2], C. Sánchez Contreras[2,4,⋆⋆], R. Neri[3], and J. Zweigle[3,⋆⋆⋆]

[1] Observatorio Astronómico Nacional (OAN), Alfonso XII 3, 28014 Madrid, Spain
e-mail: j.alcolea@oan.es
[2] Observatorio Astronómico Nacional (OAN), Apartado 1143, 28800 Alcalá de Henares, Spain
e-mail: bujarrabal@oan.es
[3] Institut de Radioastronomie Milimetrique (IRAM), 300 rue de la piscine, 38406 St. Martin-d'Hères, France
e-mail: neri@iram.fr
[4] Departamento de Astrofísica, Facultad de C. Físicas, Universidad Complutense, 28040 Madrid, Spain

Received 19 January 2001 / Accepted 6 April 2001

**Abstract.** We present high spatial resolution observations of the CO molecular emission ($J = 1{-}0$ and $J = 2{-}1$ lines) in the post-AGB bipolar nebula OH 231.8+4.2. High-quality NIR images ($J$, $H$, $K'$ bands) of light scattered by grains were also obtained. Our observations probe the bulk of the nebular material, providing maps with a resolution $\sim 1''$ of the mass distribution, both CO and NIR images being very closely coincident. The combination of the two $^{12}$CO lines has been used to measure the distribution of the kinetic temperature in the nebula, which is found to be very low, ranging between 8 K, in the outer southern clumps, and 35 K, in the central region. A relative temperature increase is found in the northernmost condensation, probably associated to a strong bow-like shock. Since velocities are also measured in CO, the dynamic parameters (kinetic momentum and energy) are also measured with high resolution. Most of the nebular mass ($\sim$0.64 $M_\odot$) is located in the central condensation and flows at expansion velocities $\leq$40 km s$^{-1}$. The rest of the gas, $\sim$0.3 $M_\odot$ almost equally distributed in the two lobes, flows along the nebular axis at high velocities, that increase proportionally to the distance to the central star reaching values as large as 430 km s$^{-1}$, as a result of a sudden acceleration happened about 770 yr ago. The general mass distribution in OH 231.8+4.2 is found to be clumpy and very elongated, with a length/width ratio reaching a factor 20 in the southern tail. In the center, however, we find a double hollow-lobe structure, similar to those found in other well studied protoplanetary nebulae. We stress the enormous kinetic linear momentum carried by the molecular nebula, about 27 $M_\odot$ km s$^{-1}$ ($5.5 \times 10^{39}$ g cm s$^{-1}$). The kinetic energy is also very high, $\sim$1700 $M_\odot$ km$^2$ s$^{-4}$ $\sim 3.4 \times 10^{46}$ erg. Given the short time during which the acceleration of the molecular outflow took place, we conclude that the linear momentum carried by the stellar photons is about a factor 100 smaller than that carried by the outflow, even if the effects of multiple scattering are taken into account. We independently argue that radiation pressure directly acting onto grains (the mechanism thought to be responsible for the mass ejection in AGB envelopes) cannot explain the observed bipolar flow, since this would produce a significant shift between the dust and gas features that is not observed. Finally, we review the uncertain nature and evolutionary status of this unique object.

**Key words.** stars: AGB and post-AGB – circumstellar matter – stars: individual: OH 231.8+4.2 – stars: mass-loss – radio lines: stars

## 1. Introduction

OH 231.8+4.2 (also known as OH 0739–14, the "Rotten Egg" nebula, the "Calabash" nebula or the "Juggler" nebula, hereafter referred to as OH 231.8) is a particularly well studied bipolar nebula around an evolved star. OH 231.8 shows very extended and elongated infrared (IR) and optical continuum images ($\sim$1 arcmin), due to the scattering by circumstellar dust grains of the light emitted by the central star (Reipurth 1987; Kastner & Weintraub 1995). These images define a clear axis of symmetry, oriented in the sky at a position angle (PA, measured from north to

*Send offprint requests to*: J. Alcolea, e-mail: j.alcolea@oan.es
⋆ Based on observations carried out with the IRAM Plateau de Bure Interferometer. IRAM is supported by INSU/CNRS (France), MPG (Germany) and IGN (Spain).
⋆⋆ Present address: Jet Propulsion Laboratory, MS 183-900 4800 Oak Grove Drive, Pasadena, CA 91109, USA; e-mail: sanchez@eclipse.jpl.nasa.gov
⋆⋆⋆ Present address: Infineon Technologies AG, Memory Products – TI CS SIM, Balanstrasse 73, 81541 München, Germany; e-mail: juergen.zweigle@infineon.com

east) of 21°, in coincidence with the direction of the nebular elongation. The orientation of this axis with respect to the plane of the sky is also very well known, $35° \leq i \leq 37°$ (Shure et al. 1995; Kastner et al. 1992), the north lobe being the closest to us. Thanks to the variability of the central star, a distance to OH 231.8 of ∼1500 pc has been determined, from the measurement of the separation between the emitting regions in the two lobes and of the delay between their two light curves, using OH masers and reflected IR light (Bowers & Morris 1984; Kastner et al. 1992). The optical continuum images are crowded with field stars, since OH 231.8 happens to lie inside the open cluster NGC 2437 (M 46). This nebula shows emission in optical atomic lines, attributed to shock excited material and responsible for a beautiful, well known picture in the shape of a calabash (Reipurth 1987; Sánchez Contreras et al. 2000a, Paper I). OH 231.8 is also an intense emitter in radio lines (Morris et al. 1987; Sánchez Contreras et al. 2000b, Paper II), that arise from a very cool ($\lesssim$20 K) and massive (about 1 $M_\odot$) molecular component, that is strongly elongated in the direction of the nebular axis (Alcolea et al. 1996; Sánchez Contreras et al. 1997). In addition to a slower expanding central component, more than 0.2 $M_\odot$ of cool gas is known to be flowing outward along the axial direction with expansion velocities larger than 40 km s$^{-1}$. The kinetic momentum associated to this axial flow is enormous, $\sim 3 \times 10^{39}$ gr cm s$^{-1}$, this value being ∼700 times the total momentum driven by the stellar radiation during the kinematic age of the flow (700–800 yr, see Sánchez Contreras et al. 1997).

OH 231.8+4.2 shows several remarkable characteristics that support its classification as a proto-planetary nebula (PPN). First, it is isolated from molecular clouds or HII complexes, and the age of the open cluster to which it probably belongs has been estimated to be ∼300 Myr (Lyngå 1987). Therefore it is very unlikely that OH 231.8 could be a young nebula. Also, its very massive circumstellar envelope (0.5–1 $M_\odot$, corresponding to a mass loss rate $\gtrsim 10^{-4}$ $M_\odot$ yr$^{-1}$) was ejected in the past by a process similar to the mass loss occurring in AGB stars. On the other hand, OH 231.8 does not show a radiatively ionized shell as planetary nebulae (PNe) do, therefore, in spite of the copious mass loss, the central star has not (yet) ejected the material surrounding its hot core, in agreement with the late spectral type of the central star (M9 III, see Kastner et al. 1998 and Paper I). Moreover, the axial symmetry of the nebula is very characteristic of many PPNe, but is very rarely found in AGB envelopes. The increase of the axial expansion velocity with the distance to the center, and the very clear signs of shocks along the symmetry axis (probably related to the axial acceleration of the nebula), are also distinct signatures of the PPN stage (Bujarrabal et al. 1998a).

On the other hand, OH 231.8 also shows peculiar properties unexpected in a PPN. In particular, the spectral type of its central star QX Pup, M9 III, does correspond to AGB sources rather than to post-AGB sources. In addition, it has been claimed that QX Pup also shows a weak UV excess (Cohen et al. 1985), which could indicate the presence of a hot companion or a peculiar photospheric structure. However, we have mentioned the very massive and fast molecular flow found in OH 231.8. We have also mentioned the enormous bow of shock-excited gas in the south lobe (much hotter than the CO emitting gas), extending over about $5 \times 10^{17}$ cm. The whole shocked structure and CO cloud occupy more than $10^{18}$ cm. These properties, that are surprising even for an object evolving toward the PNe stage, are incompatible with what is usually observed in envelopes around M-type stars. Summarizing, apparently the star at the center of OH 231.8 is in the AGB, although the nebula clearly show characteristics of a post-AGB object, a paradox which makes difficult the determination of the evolutionary status of the object.

One possible solution to this paradox could be that the atmospheric line features of post-AGB stars cannot be interpreted in terms of the usual spectral-type ladder, and therefore we could not deduce from the optical spectra of QX Pup that the star is red giant. However, it is also possible that OH 231.8 is following a non standard evolutionary path, perhaps due to the presence of a companion. The OH 231.8 nebula would then be similar to other PPNe, from the dynamical point of view, while its central star QX Pup would still be in the AGB phase. If this is the case, it is possible that the sample of objects we classify as PPNe is significantly contaminated by stars following an anomalous evolution, which could be very rare but observationally conspicuous. OH 231.8 would then be a clue to understand the classification of this kind of stars. Another possibility, of course, could be that the bipolarity of the circumstellar material develops at the very end of the AGB, while the central star is still a red giant. In this scenario OH 231.8 will not be a peculiar object, but a source right at the precise point, in its fast evolution toward the PNe phase, in which both AGB and post-AGB properties can coexist. Would this be the case, the study of OH 231.8+4.2 should provide with fundamental pieces of information to improve our knowledge on these late stages of the stellar evolution.

To help in better understanding the properties of the OH 231.8 nebula, we have conducted a series of (ground-based) arcsec. resolution observations of the circumstellar envelope of OH 231.8 in the optical, the near infrared (NIR) and in mm-wave molecular lines. In the optical, we have performed broad-band imaging, and long-slit spectrometry and imaging of shocked excited atomic lines to probe the highly excited material; these results are presented in Paper I (Sánchez Contreras et al. 2000a). The results of the interferometric observations of mm-wave lines of molecular species other than CO (namely, $^{28}$SiO, HCO$^+$, H$^{13}$CN, SO, and NS), which help us in understanding the peculiar and very active chemistry in the envelope of this source, are presented in Paper II (Sánchez Contreras et al. 2000b). Here in Paper III, we will present our results from interferometric observations of the $J = 1{-}0$ and $J = 2{-}1$ rotational lines of $^{12}$CO and

**Table 1.** Magnitudes adopted for the calibrators used in the NIR observations.

| | — mag — | | |
|---|---|---|---|
| | $J$ | $H$ | $K'$ |
| HD 62388 | 8.742 | 8.735 | 8.721 |
| HD 114895 | 8.276 | 8.166 | 8.144 |

broad-band NIR images. The observation of the mm-wave emission of CO lines is the basic tool to probe the bulk of the nebular material in PPNe, due to their low excitation requirements, while the gas emitting in atomic lines only represents a very small fraction or the total mass (see e.g. Bujarrabal et al. 1998b). The interferometric observations of CO lines, with both high spatial and spectral resolution, allows a very precise determination of the structure, kinematics, excitation, and other physical parameters of the molecular envelope, and from them the kinetic momentum and energy. The nebular images in the infrared, due to the scattering of the emission of the central star and its immediate surroundings by circumstellar dust grains, also trace the mass distribution in an independent way, since scattering by dust works regardless of the excitation conditions in the nebula. The details of the CO and NIR observations and the data reduction processes are explained in Sect. 2. In Sect. 3 we present the results directly obtained from the observations, that will be also compared with the optical and molecular data presented in papers I and II. Estimations of the excitation and kinetic temperature of the nebula, its mass distribution, momentum and kinetic energy, and other physical parameters of OH 231.8 will be presented in Sect. 4. Finally, in Sect. 5, we will summarize the main conclusions of this paper and address the problem of the nature and the evolutionary status of OH 231.8.

## 2. Observations and data analysis

### 2.1. Near infrared observations (NIR)

The broad-band NIR observations were done using the IRAC-2b camera on the ESO/MPI 2.2 m telescope at La Silla, Chile, on the 25th and 26th of April, 1997. We observed OH 231.8 in the three broad band filters $J$, $H$, and $K'$ (at 1.25, 1.65, and 2.15 $\mu$m respectively). The IRAC-2b camera is equipped with a 256×256 NICMOS-3 array, which at the 2.2 m telescope operating in the LB optic mode results in a pixel size in the sky of $\sim 0\farcs28$, and a field of view of $\sim 71'' \times 71''$. The images have been corrected for flat field, dark current, and sky background emission in the standard way. The absolute calibration of the intensity scale was derived from observations of the two standard stars HD 62388 and HD 114895, for which we quote in Table 1 the magnitudes adopted at the three observed bands. Absolute positioning and orientation of the images has been performed using several field stars, by comparing their location with respect to those in optical images for which precise astrometry, based on GSSC sources, has been also performed by us (Paper I); we believe that the final NIR images have an absolute positioning accuracy better than $1''$. The FWHP of the PSF in the NIR images is $\sim 1\farcs2$ for the $J$ and $H$ filters, and $\sim 1\farcs0$ for $K'$. The resulting images obtained for the three filters, and for the colors $[J-H]$ and $[H-K']$, are shown in Fig. 1.

### 2.2. Interferometric observations of $^{12}$CO

The molecular line observations of $^{12}$CO have been performed with the mm-wave interferometer at Plateau de Bure (PdB), located in the French Alps near Gap. This instrument, operated by IRAM, presently consists of 5 antennas of 15 m in diameter, equipped with dual channel receivers for simultaneously observing in the 3 and 1.3 mm bands. The receivers consist in SIS mixers cooled with closed cycle Helium compressors (a more detailed description of the instrument can be found in Guilloteau et al. 1992). We simultaneously observed the $J = 1{-}0$ and $J = 2{-}1$ rotational lines of $^{12}$CO, at rest frequencies of 115 271.2 and 230 538.0 MHz respectively. The $J = 1{-}0$ line was tuned in single side band (SSB) mode in the upper side band (USB) of the 3 mm receiver, with a typical SSB system temperature (SSB $T_{\rm sys}$) of 550 K, while the $J = 2{-}1$ one was tuned in double side band (DSB) mode in the lower side band (LSB) of the 1.3 mm receiver (SSB $T_{\rm sys} \sim 500$ K). In addition to the two lines of $^{12}$CO, we have also detected the $^2\pi_{1/2}$ $J = 5/2{-}3/2$ $e$-parity quintuplet of NS between 115 156.9 and 115 191.3 MHz, which happens to lie in the band covered by the spectral backend we used with the 3 mm receiver: this represents the first detection of circumstellar NS, see Paper II for more details. We have also detected the continuum emission at 2.6 and 1.3 mm from OH 231.8, these observations will be discussed elsewhere.

From previous (single-dish) observations of this source, carried out with the IRAM 30 m MRT at Pico de Veleta (Sierra Nevada, Spain), we knew that the CO emission was elongated in the direction of the nebular symmetry axis, with a total length or $\sim 50''$ (see Sánchez Contreras et al. 1997). At 115 GHz, the primary beam (HPBW) of the Plateau de Bure antennas is only $\sim 42''$; therefore, for properly mapping the whole envelope we had to perform our interferometric observations in the so called mosaicing mode, i.e. pointing the telescopes at several positions in the nebula. We did observations at three positions along the nebular axis, at east and north offsets of $(+4\farcs6, +11\farcs2)$, $(-2\farcs9, -8\farcs4)$, and $(-10\farcs4, -28\farcs0)$, with respect to the coordinates adopted for the central star, which are $07^{\rm h}42^{\rm m}16\fs93$, $-14^\circ 42' 50\farcs2$ (J2000 equinox). These coordinates are those derived for the SiO maser emission, which is believed to lie very close to the central star QX Pup (see Paper II). In Fig. 1f, we plot a view of the nebula in the optical and the primary beam coverage at the two transitions. As it is shown in this figure the mosaicing coverage at 230 GHz is not optimal. The angular separation between the three points in our mosaic is $21''$, just the HPBW of the primary beam of the

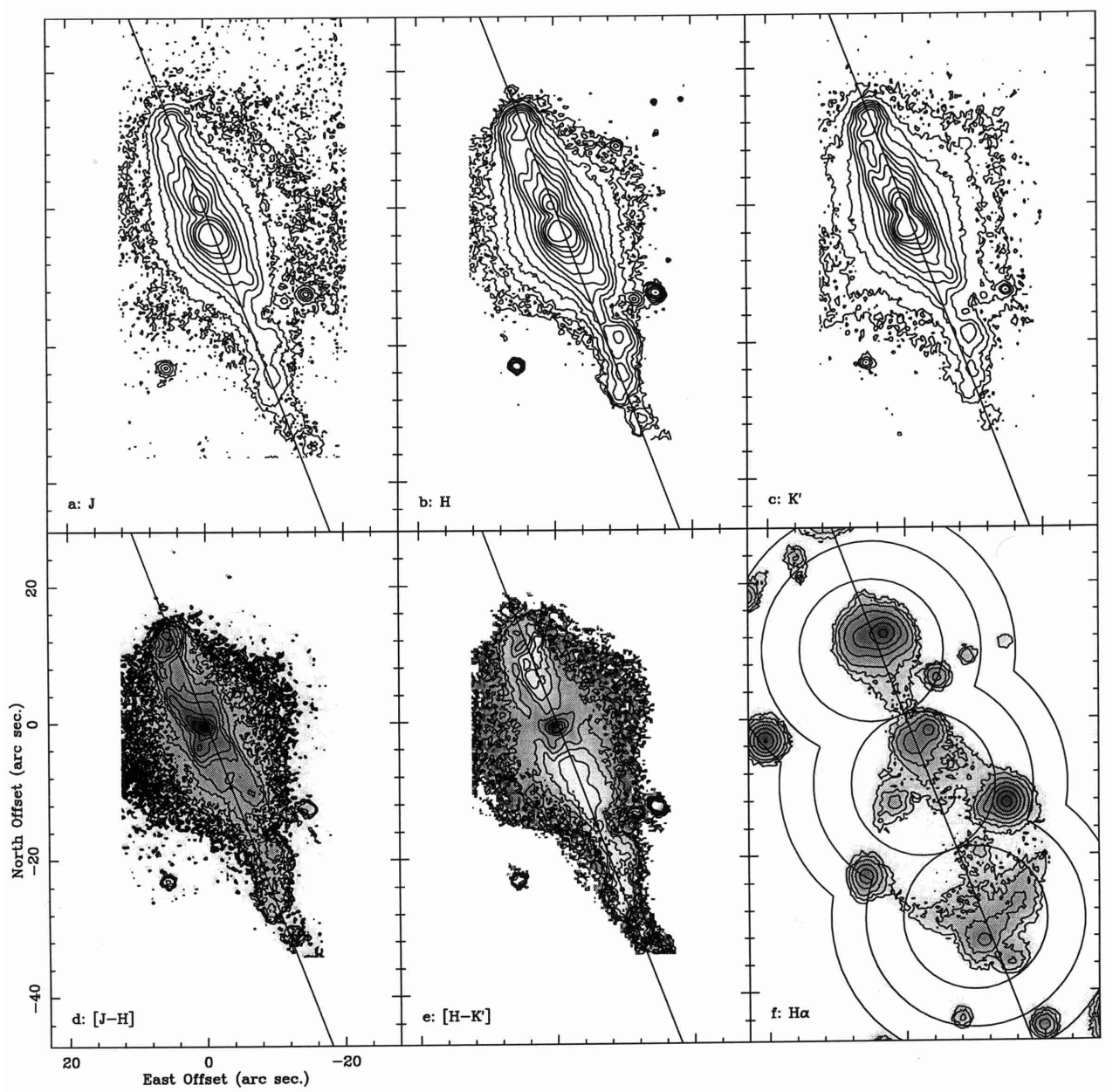


**Fig. 1.** Broad-band NIR images and colors of OH 231.8+4.2. **a)** $J$-band image: contours are 0.15, 0.25, 0.5, 1.0, 2.0, 4.0, 8.0, 15, 25, and 50% of the maximum ($8.2 \times 10^{-26}$ erg s$^{-1}$ cm$^{-2}$ Hz$^{-1}$ arcsec$^{-2}$). **b)** $H$-band image: contours are 0.03, 0.05, 0.08, 0.15, 0.25, 0.5, 1.0, 2.0, 4.0, 8.0, 15, 25, and 50% of the maximum ($3.3\times10^{-25}$ erg s$^{-1}$ cm$^{-2}$ Hz$^{-1}$ arcsec$^{-2}$). **c)** $K'$-band image: contours are 0.05, 0.08, 0.15, 0.25, 0.5, 1.0, 2.0, 4.0, 8.0, 15, 25, and 50% of the maximum ($1.2 \times 10^{-24}$ erg s$^{-1}$ cm$^{-2}$ Hz$^{-1}$ arcsec$^{-2}$). **d)** $[J-H]$ color image displaying the regions of larger extinction in darker colors: contours are −0.6 to 1.6 by 0.2 mag. **e)** same as before but for the $[H-K']$ color: contours are 0.25 to 1.75 by 0.25 mag. **f)** H $\alpha$ image from Sánchez Contreras et al. (2000a, Paper I): contours are 0,09, 0.15, 0.25, 0.5, 1.0, 2.0, 4.0, and 8.0% of the maximum ($1.1 \times 10^{-13}$ erg s$^{-1}$ cm$^{-2}$ arcsec$^{-2}$, not shown in the plot); in this image all compact components are field stars. In all the panels we plot the symmetry axis of the nebula, oriented at a PA $\sim 21°$. The origin of the maps is located at the assumed position for the central star (see Sect. 2.2). In the last panel **f)** we also show the coverage for the interferometric maps (see Sect. 2.2): from inside to outside, the three circles covered by the $^{12}$CO $J = 2{-}1$ observations at half power of the primary beam; the region covered by $^{12}$CO $J = 2{-}1$ observations at 20% power of the primary beam; the region covered by $^{12}$CO $J = 1{-}0$ observations at half power of the primary beam.

individual antennas at 230 GHz. Therefore, to properly map the whole nebula in the $J = 2{-}1$ line of $^{12}$CO, in some regions we have used factors larger than 2 in order to correct for the primary beam taper at 230 GHz (we have considered points down to 20% of the maximum power of the primary beams).

The observations were performed in two seasons, always using standard five-antenna configurations at PdB.

In the 1996–1997 winter period, we observed in the 5D, 5C1, 5C2 and 5B1 configurations. One year later, the 5B2 configuration was added mainly for improving the resolution at 3 mm in the north-south direction. The data were calibrated in amplitude and phase by observing strong and point-like quasars, and the radio-continuum emission of the H II region associated to the post-AGB source CRL 618. For the phase corrections we observed the quasar 0609−157, and also 0730−116 in some configurations (for which the following J2000 coordinates were assumed respectively: $06^{\rm h}09^{\rm m}40\overset{\rm s}{.}9497$, $-15°42'40\overset{''}{.}674$, and $07^{\rm h}30^{\rm m}19\overset{\rm s}{.}1125$, $-11°41'12\overset{''}{.}600$; see the VLA calibrator list). These two quasars were also used as secondary amplitude calibrators. To fix the absolute intensity scale, observations of CRL 618 and the strong quasar 3C 273 were also carried out; these sources are regularly monitored at Plateau de Bure (PdB) and Pico de Veleta (PdV) observatories. The RF passband calibration was performed using the observations of 3C 273.

As backend a digital correlator was used. This correlator was set up to observe the $J = 1{-}0$ line with a spectral resolution of 1.63 km s$^{-1}$ and the $J = 2{-}1$ line with 3.25 km s$^{-1}$, although to improve the signal to noise ratio we will present results for both lines from data with a resolution of only 6.5 km s$^{-1}$. In addition, the continuum emission of the source at 115 and 231.5 GHz was also recorded from those channels of the correlator were line emission was not found (spare units of the correlator and the whole USB of the 1.3 mm receiver). The recorded data were calibrated as described before and converted into *uv*-tables using the CLIC program included in the GAG software package. These tables were converted into maps, and then CLEANed following the Clark method, using the standard routines developed for PdB mosaics in the GAG software package. In this mapping procedure, we have limited the mapped area to those points requiring a correction for the primary beam taper lower than a factor of 2 and 5, for the $^{12}$CO $J = 1{-}0$ and $J = 2{-}1$ lines respectively (see Fig. 1f). Mapping was performed using natural weighting for the two lines. After the cleaning, the maps were restored using the Gaussian CLEAN beam which resulted from the fitting of the central peak of the dirty beam. The HPBW of those clean beams are, for the $J = 1{-}0$ line $3\overset{''}{.}5{\times}1\overset{''}{.}5$ (the mayor axis being at a PA of 38°), and $1\overset{''}{.}5{\times}0\overset{''}{.}7$ (at a PA of 12°) for the $J = 2{-}1$ line.

The maps obtained for the two CO lines are shown in Figs. 2–5. In Fig. 2 we present the maps of the $J = 1{-}0$ line emission for the different velocity channels. Similar results for the $J = 2{-}1$ line are shown in Fig. 3 (see also Fig. 7). In Fig. 4 we show maps of the integrated emission of the two transitions, in comparison with optical and NIR images. In Fig. 5, we plot the velocity position diagrams for cuts along the direction of the axis of symmetry of the nebula (PA 21°), of the $J = 1{-}0$ and $J = 2{-}1$ $^{12}$CO lines, together with H$\alpha$ (from Paper I) for comparison.

From the maps obtained, we have computed the total $^{12}$CO $J = 1{-}0$ and $J = 2{-}1$ spectra for the whole nebula. These spectra have been compared with those obtained from the single dish observations previously performed with the PdV IRAM 30 m MRT (total fluxes for the same velocity ranges). For the $J = 1{-}0$ line we found no significant discrepancies between the spectra obtained with the two instruments, and therefore we conclude that no flux is lost in the interferometric observations at 115 GHz. On the contrary, the PdB total spectrum for the $J = 2{-}1$ line has been found to be between 0.5 and 1.1 times (depending on which velocity channel we consider) that obtained with PdV. This could be due to an inconsistent calibration between the two instruments, or could also indicate that the $^{12}$CO $J = 2{-}1$ emission has been partially resolved out in the interferometric observations at 230 GHz. This resolved out flux should originate from a spatially extended component not properly sampled by our *uv*-coverage at 1.3 mm. If this is the case, this component can not be very extended since it has not been resolved out in the $J = 1{-}0$ line. Anyhow, thanks to the larger extent that this component would have, the flux values measured (at any pixel) in the $^{12}$CO $J = 2{-}1$ maps should be much less affected by this loss of signal than the spatially integrated total flux. We estimate that the measured brightness temperature is reliable, within an uncertainty range of $\sim\pm50\%$. Moreover, the morphology revealed in the maps should be about correct, except for the possible existence of an extended low-level component.

Anyhow, to further test whether the missing flux problem is due to a resolved out component, we have performed additional $^{12}$CO $J = 2{-}1$ maps which include the (zero-spacing) results from our maps obtained with the 30 m telescope. To do this, the single-dish maps have been Fourier transformed and the resulting *uv*-data have been merged with those from the interferometric observations. The merged *uv*-data have been transformed into maps and CLEANed as explained before. In spite of the fact that the maps obtained in this way include the zero-spacing information, the lost flux problem is not fully solved; we only recover about 50% of the previous missing flux. Apparently, the problem of the missing $^{12}$CO $J = 2{-}1$ flux in OH 231.8+4.2 is more complex than just having some features partially resolved out; it is possible that we also have some problems with the calibration (it is a rather low declination source for PdB) and/or with the (large) correction factors used in some parts of the mosaic because of the poor coverage in this line. In addition, in these combined PdV & PdB maps the spatial resolution and sensitivity are degraded. Because of this we will not use these merged $J = 2{-}1$ maps; we will only use those not including the PdV observations. We recall that these maps are correct for studying the morphology and kinematics of the nebula; only those calculations that need values of the brightness temperature of the $J = 2{-}1$ line, $^{21}T_{\rm B}$, are somewhat affected by the lost flux problem. In these cases we will try to correct that effect by multiplying the data by the appropriate factor (see Sect. 4). With these corrections, we believe that the results we derive from our $^{12}$CO interferometric data are valid.

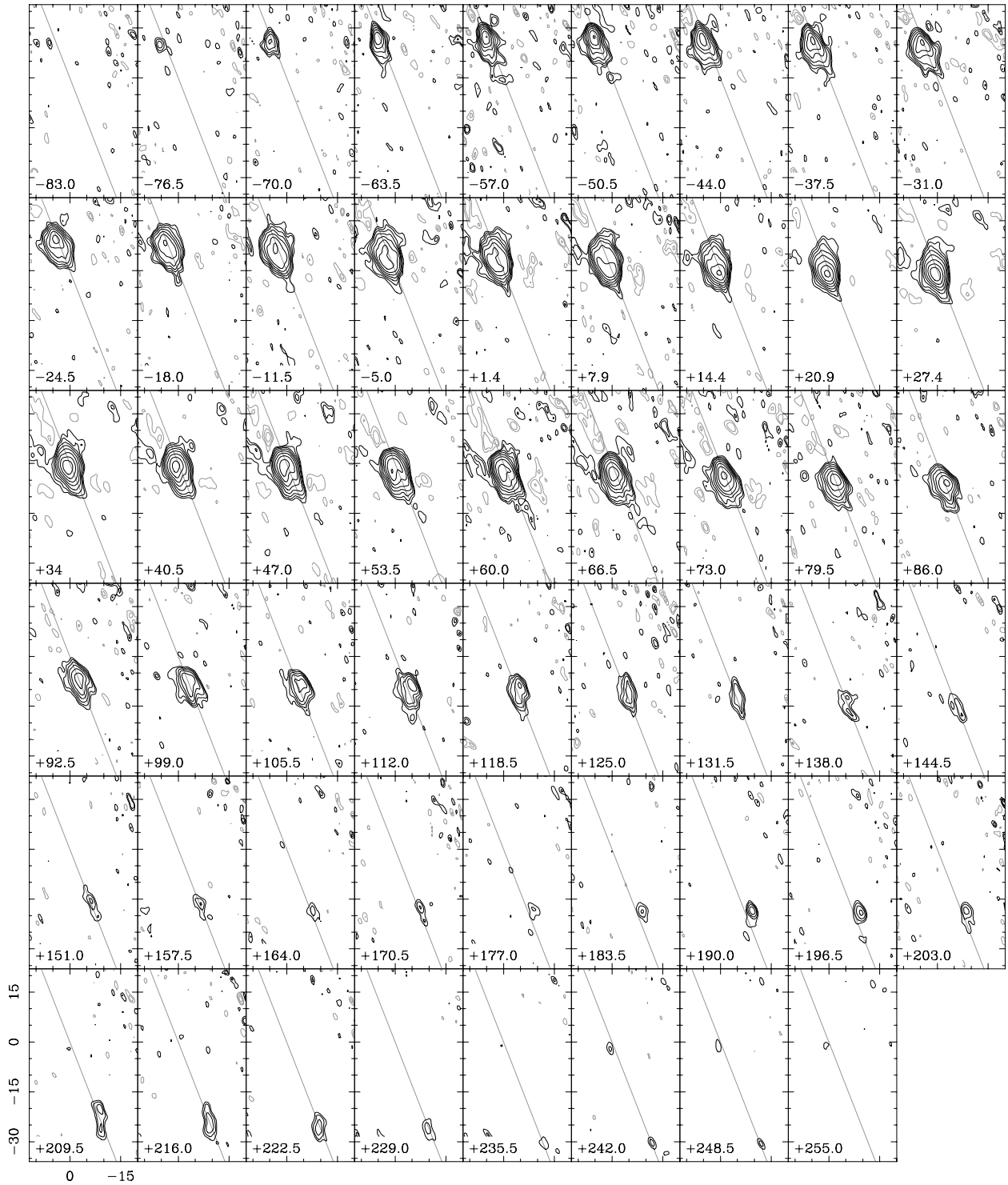


**Fig. 2.** Plateau de Bure maps of OH 231.8+4.2 in the $^{12}$CO $J = 1{-}0$ line. In each panel, we plot the emission of $^{12}$CO $J = 1{-}0$ within a 6.5 km s$^{-1}$ wide channel, centered at the LSR velocity (in km s$^{-1}$) shown in the bottom left corner. Contours are spaced logarithmically: $11^{n/6}$ Jy·beam$^{-1}$, for $n = -11$ to 2 by 1. No contours are plotted below 1/25 of the maximum in each panel. Negative contours are shown in light grey. East and North offsets (in arcsec) are with respect to the assumed position for the central star (see Sect. 2.2). The diagonal line shows the nebular axis of symmetry.

## 3. Observational results

### 3.1. NIR observations

The NIR broad-band and color images of OH 231.8+4.2 presented in Figs. 1a–f show a reflecting nebula in which three main components can be distinguished: the bright bipolar nebula (the only one of the three components known before our observations), a southern weak tail extending to at least 38″ from the center, and a yet weaker quasi-spherical halo with a radius $\gtrsim$12″, surrounding the central parts of the nebula.

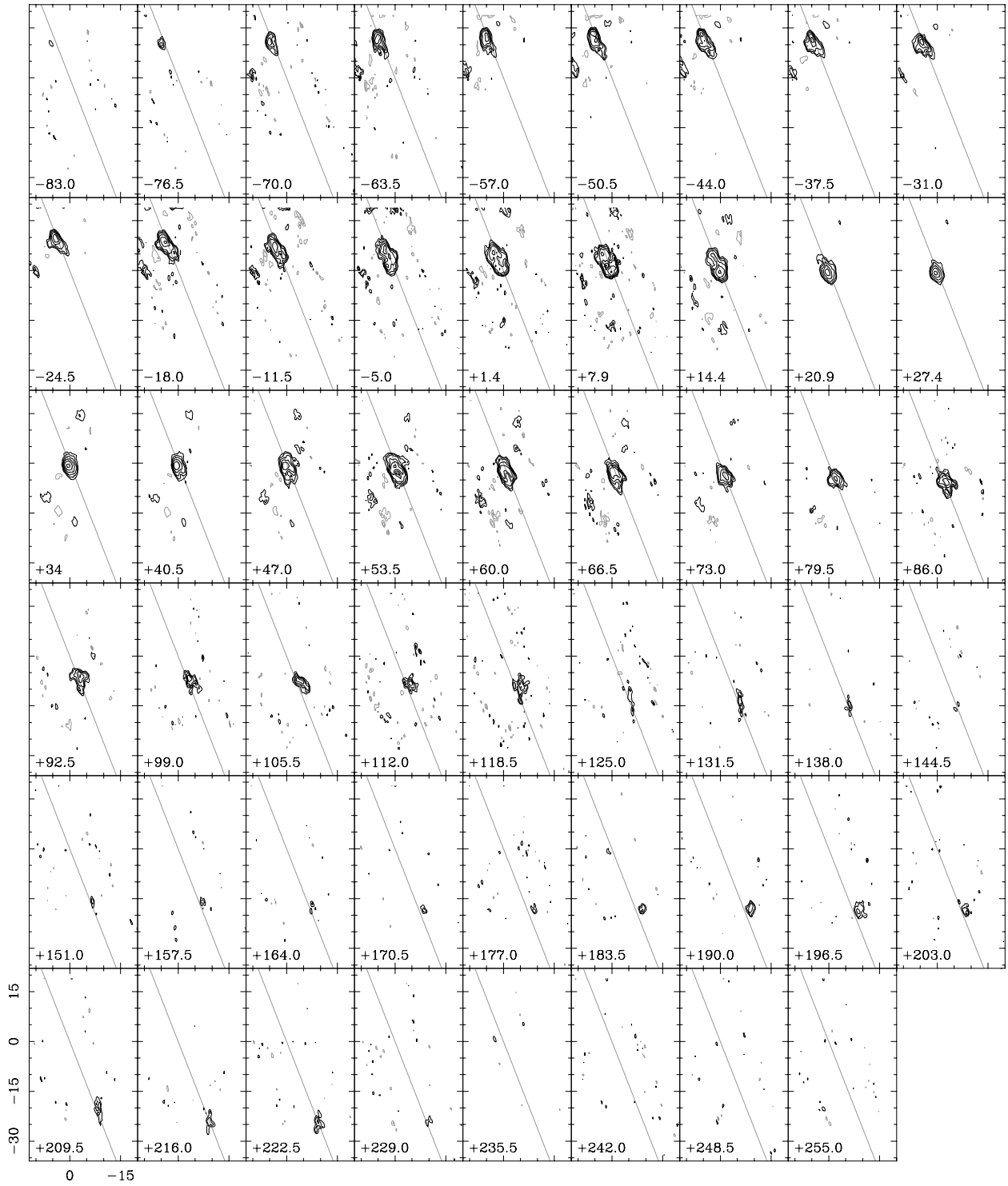


**Fig. 3.** Same as Fig. 2 but for the $^{12}$CO $J = 2{-}1$ line. Contours are spaced logarithmically: $10^{n/6}$ Jy·beam$^{-1}$, for $n = -11$ to 2 by 1. No contours are plotted below 1/7.5 of the maximum in each panel (sse also Fig. 7).

The previously known bipolar reflecting nebula (see Kastner et al. 1998 and references therein) is the brightest part of OH 231.8 in the NIR. The two lobes are clearly not symmetric. The northern one presents a much richer structure: the end of the lobe consisting of several knots, unresolved in our observations, and the lobe itself shows the presence of two filament-like structures running from the base of the lobe up to the north end. One of these filaments, which is better shown in the $J$-band image, lies along the nebular axis; the other filament delineates the east limit of this north lobe and appears more conspicuously in the $K'$-band image (Fig. 1c). A hint of a possible (weaker) third filament, delineating the west border of the lobe, is also observed. (These structures have been

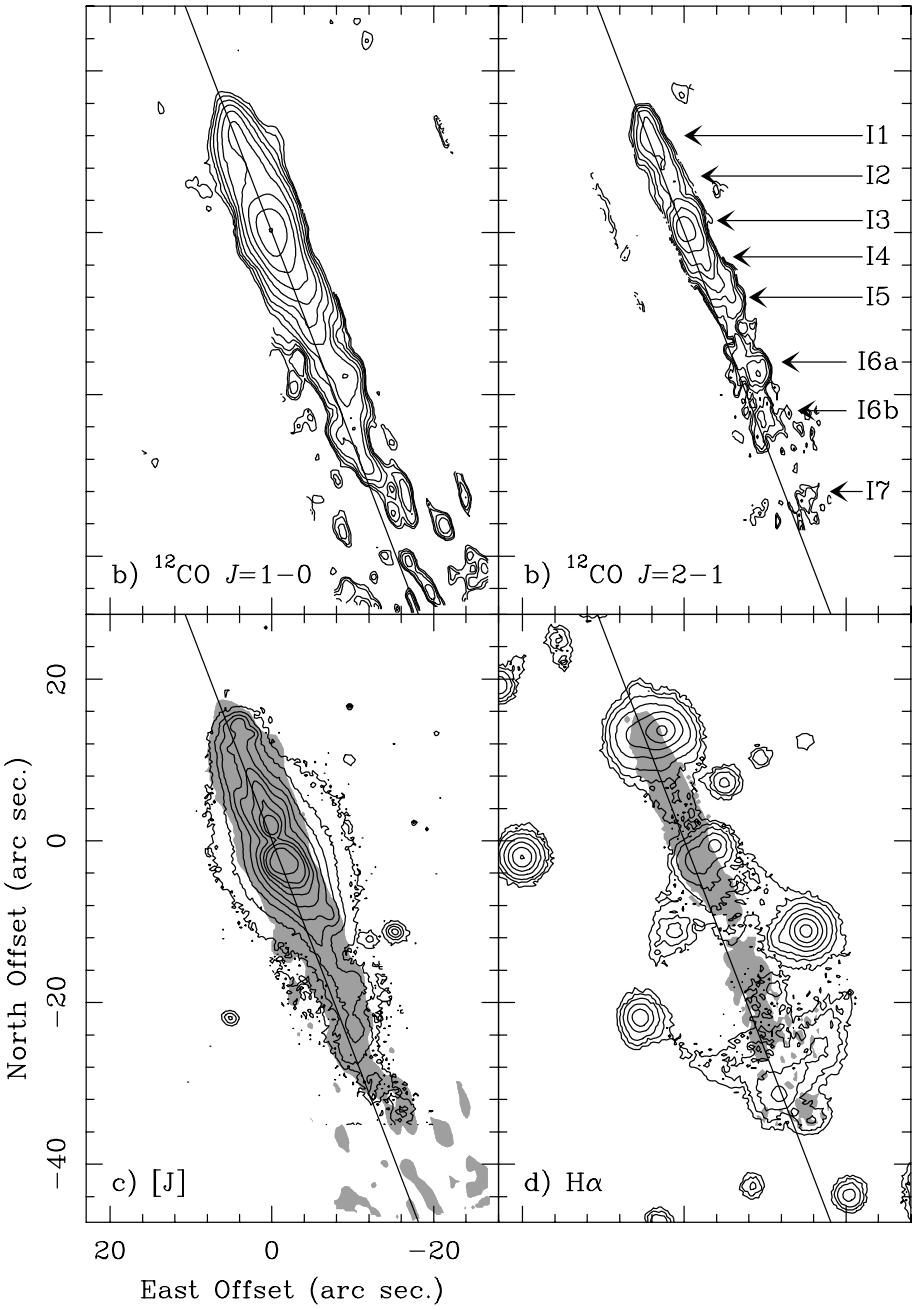


**Fig. 4.** Integrated $^{12}$CO emission in the $J = 1{-}0$ and $J = 2{-}1$ lines from the PdB interferometric maps. **a)** Integrated emission of the $J = 1{-}0$ line. Contours are spaced logarithmically (five contours per decade): 0.25, 0.4, 0.63, 1.0 (only in the south tail), 1.6, 2.3, 4.0, 6.3, 10, 16, 23, 40, and 63 Jy beam$^{-1}$ km s$^{-1}$. **b)** Idem for the $J = 2{-}1$ line. Contours are spaced logarithmically (five contours per decade): 0.63, 1.0, 1.6 (only in the south tail), 2.3, 4.0, 6.3, 10, 16, 23, 40, and 62 Jy beam$^{-1}$ km s$^{-1}$. In panel **b)** we also show the location of the emitting regions I1 to I7 in which we have divided the nebula to estimate its mass, momentum and kinetic energy (see Sect. 4). **c)** sketch of the total $J = 1{-}0$ emission (gray shade) in comparison with the $J$-band image from Fig. 1a. **d)** sketch of the total $J = 2{-}1$ emission (gray shade) in comparison with the H$\alpha$ image from Fig. 1f.

confirmed by the much more detailed picture of this nebula taken with the NICMOS-2 camera on-board the HST (see Bieging et al. 2000).)

It is also noticeable the fact that the south lobe is brighter than the north one in all NIR images. A priori, this is not expected from the orientation of the nebula. From the CO observations we know that the masses of the two lobes are similar ($\sim$0.1 $M_\odot$; see Table 2), therefore, since the south lobe is receding form us, one should expect, near the star, larger extinction and less intense NIR emission in this lobe, which would be partially obscured by the thick dusty equatorial belt dividing the two lobes typical of bipolar reflecting nebulae. The existence of this belt and its orientation is on the other hand confirmed by the images, where the minimum between the two lobes, in coincidence with the region of larger extinction, is located $\sim$1″ to the south of the position of the central star. This reversal of the relative strength of the two lobes can be explained if this equatorial belt is small, obscuring only the south lobe very close to the star, and if the two local NIR maxima in the images are mainly due to light scattered in the walls of two hollow lobes. (We will further justify the presence of these hollow lobes.) Under these assumptions, it is possible to have the south lobe brighter than the north one since, due to the orientation of the nebula, the front wall of the south lobe is closer to the star than the front wall of the north lobe. In this case, and if the dusty walls of the reflecting lobes are optically thick (we do not see the rear side of both lobes), it is possible to have larger flux for the scattered light from the lobe receding from us.

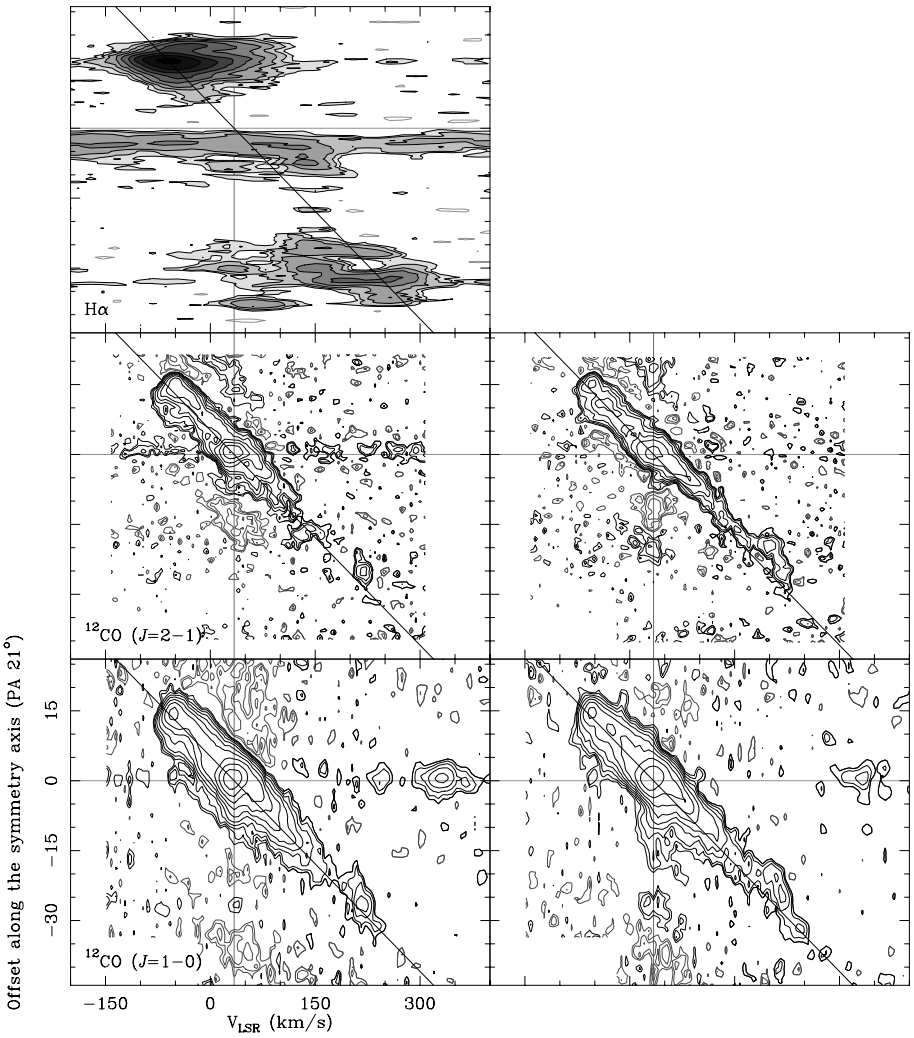


**Fig. 5.** On the left side, position vs. velocity diagrams for cuts along the symmetry axis of OH 231.8 for the $^{12}$CO $J = 1-0$ (bottom) and $J = 2-1$ (middle) lines. Positive offsets in the ordinate axis are to the northeast (at PA $= 21°$), while the velocity is in km s$^{-1}$ with respect to the LSR. For comparison we also reproduce the long-slit H $\alpha$ observation taken with the same orientation (from Paper I). To easy the comparison we have drawn in the panels the velocity gradient observed in the molecular emission (6.5 km s$^{-1}$ per arcsec), the center of the nebula, and the systemic velocity. Horizontal strips near $0\farcs0$ ($J = 1-0$ and $J = 2-1$ lines) and $-3\farcs5$ (H $\alpha$) mark the location of the continuum emission. (The local maxima at $+350$ km s$^{-1}$ and $0\farcs0$ in the $^{12}$CO $J = 1-0$ plot shows the detection of the NS line (see Paper II).) Levels are spaced logarithmically in all three plots. On the right side, position vs. velocity diagrams for cuts parallel to symmetry axis but $\sim 0\farcs75$ to the northwest, passing through all the $^{12}$CO emission clumps on the south tail. Axis and contours are the same as in the corresponding plots on the left.

The $[H - K']$ image is clearly axially symmetric, revealing the presence of regions of lower extinction at the center of the two lobes. Assuming cylindrical symmetry, the presence of these regions of lower extinction inside the lobes clearly demonstrates that the two lobes are hollow, the scattered light mainly emanating from the corresponding walls. On the contrary, the $[J-H]$ image shows a point symmetric appearance, due to a brighter emission along an S-shaped structure. (Due to the dependence in wavelength of the coefficients of true extinction and scattering by dust particles, it is expected that the $[H - K']$ color better depicts the dust density distribution in the nebula, while the $[J - H]$ one is more dependent on the way the starlight escapes from the very opaque central regions.)

As we have mentioned, due to the large field of view and deepness of our NIR imaging, in addition to the bright reflecting lobes divided by the equatorial dust belt, we also detect two other remarkable structures previously unknown. At the end of the south lobe, we detect a long curled tail, consisting of several ($\sim$5) clumps of $\sim 2''$ in size, extending to (projected) distances of at least $38''$. (We can not rule out that the tail proceeds farther out, since the NIR image which extends southernmost, the $J$-band, ends at $40''$ from the center, see Fig. 1.) Our images have also revealed the presence of an extended component of low level emission. This component, centered at the star position, is nearly spherically symmetric and has an outer radius of $\gtrsim 12''$ ($\sim 2.7 \times 10^{17}$ cm). The long south tail is the NIR counterpart of the molecular outflow detected in CO, which is also much larger on the south than in the north (see next section). On the contrary, the extended spherically symmetric component has no molecular counterpart, or is extremely weak. The spherical symmetry of this latter structure, in spite of the fact that the starlight is more obscured along the equatorial plane of the nebula, suggest that it is due to a second order scattering. This result is also supported by the lower degree and orientation (pointing to the star) of the linear polarization of the NIR light outside the lobes (Kastner & Weintraub 1995). The relatively red color of this component, that is more conspicuous at longer wavelengths, points out that the stellar light suffers a severe extinction before it reaches this part of the nebula.

From a cut of the $K'$-band image through the star along a direction perpendicular to the nebular axis, we find that for radii larger than $4''$–$5''$, the NIR flux shows a $1/r^{\alpha}$ dependence with the distance to the center, with $\alpha \sim 2$–$3$ (see Fig. 6). To correctly interpret NIR flux

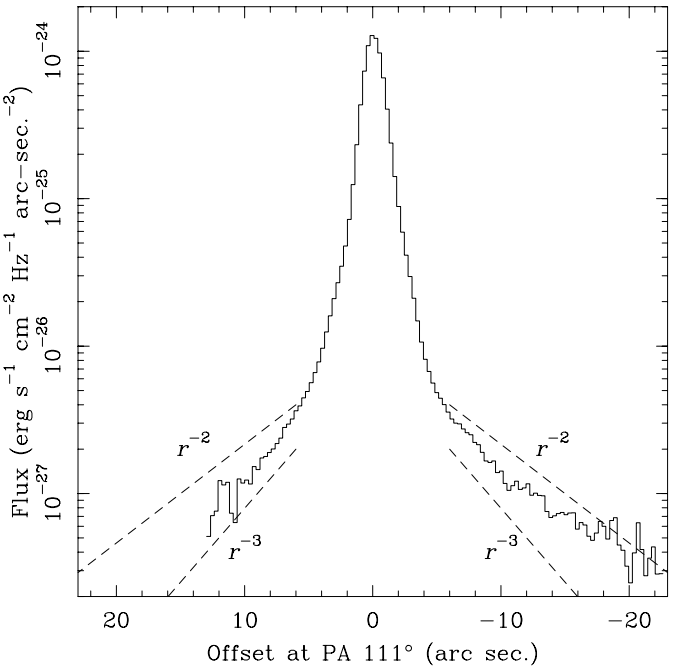


**Fig. 6.** A cut of the K′-band image along the equatorial direction of the nebula (at PA = 111°, i.e. positive offsets are to the southeast), showing that farther than 4–5″ the flux follows a $1/r^{\alpha}$ dependence, with $\alpha \sim$ 2–3. See also Sect. 3.1.

dependences in terms of density laws, and since we are analyzing scattered light, we should first correct for the light intensity dilution. Since the emission of this round halo is rather due to second order scattered light, we should consider the dilution of the first order scattered light, which emanates mainly from the two strong reflecting lobes. For an elongated object like ours, one should expect this correction to be between $\sim 1/r$ and $\sim 1/r^2$. (The dilution of a flux field emanating from a point source is $\sim 1/r^2$, but from an infinite long wire is $\sim 1/r$; here we should be in a intermediate case.) In addition, for a spherically symmetric shell with a density proportional to $1/r^2$, i.e. a constant mass loss, the optical thickness integrated along the line of sight is proportional to $\sim 1/r$. Therefore, under this scenario the scattered light intensity should vary as $1/r^{\sim 2.5}$, as it is observed. This result strongly suggests that this component must be the remnant of a constant mass loss ejected in the past. Taking into account the size of this halo and assuming an AGB expansion velocity of 8 km s$^{-1}$ (see later), we estimate that this period of constant mass loss started, at least, ∼11 000 yr ago, ending about 6500 yr later (∼4500 yr ago). For radii closer than 5″, the dependence of the flux with the distance is much steeper, showing that very probably the mass loss started to increase significantly some 4500 yr ago.

Finally, we want to point out that, although in the north the shape of the nebula in the NIR resembles very much its optical appearance, this result does not hold for the south lobe. Here, the large H $\alpha$ emitting bubble explained in terms of shock fronts (see Paper I) is not present at all in the NIR broad-band images, in spite of their deep sensitivity. On the contrary, as we will see next, the NIR emission is extremely well correlated with the molecular line emission detected in $^{12}$CO.

### 3.2. Molecular line data

As expected from the previous single dish observation, it can be seen in Figs. 2–4 that the $^{12}$CO emission in OH 231.8 is confined to a very narrow region along the symmetry axis of the nebula. Its total extent is 57″ along this axis, and <5″ in the perpendicular direction. The maximum CO intensity is attained approximately at the assumed star position (always at the origin in our maps) and at an LSR velocity of ∼34 km s$^{-1}$. We recall that we have adopted as the position of the central star QX Pup the coordinates derived for the SiO maser emission (Paper II). The maxima of both $^{12}$CO lines at +34 km s$^{-1}$ LSR is ∼0.″4–0.″5 to the north-east, as it also happens to the maximum of the map of the 3 mm continuum emission (Paper II). All these coordinates are compatible, considering the expected errors for the determination of absolute coordinates in the different maps. We have detected $^{12}$CO emission in the range −90 to +255 km s$^{-1}$ (LSR) in both $J = 1{-}0$ and $J = 2{-}1$ lines. (We have tentatively detected emission up to 287.5 km s$^{-1}$ in the $J = 1{-}0$ transition.) Channel by channel, the CO emission is very compact in comparison with the total extent of the nebula; for each velocity, sizes of ∼3″–4″ are typical in the $J = 1{-}0$ line and somewhat smaller for the $J = 2{-}1$ one.

The kinematics of the CO emission is dominated by a strong velocity gradient along the nebular axis. This result was previously known from the observations performed with the Pico de Veleta telescope (see Alcolea et al. 1996; Sánchez Contreras et al. 1997), but it is much better displayed in the interferometric maps. The position vs. velocity diagrams for cuts along the symmetry axis, shown in Fig. 5, also point out that this velocity gradient is nearly constant; from these cuts we derive a (projected) value for the gradient of 6.5 km s$^{-1}$ per arcsec. for the two lines. This value agrees with the previously computed for this source from the single-dish observations of CO and other molecules (Sánchez Contreras et al. 1997), and from the interferometric observations presented in Paper II. It also agrees with the large scale velocity gradient found in the long-slit observations of atomic lines (Paper I; see also Fig. 5). This velocity gradient of 6.5 km s$^{-1}$ per arcsec. is very similar to the one found for M 1–92, another young PPN showing this peculiar kinematics too (Bujarrabal et al. 1998a). For a systemic velocity of +34 km s$^{-1}$, and assuming that the CO flow is moving along the axis of the nebula, which is inclined 36° (see Sect. 1) with respect to the plane of the sky, we conclude that in OH 231.8 the molecular envelope is expanding at deprojected velocities up to 210 km s$^{-1}$ in the north lobe, and up to 376 km s$^{-1}$ in the south (430 km s$^{-1}$ for the tentatively detected southernmost clump). These expansion velocities are, up to date, the largest known

for molecular gas in AGB and post-AGB sources. The deprojected value of the velocity gradient is 8.9 km s$^{-1}$ per arcsec, which adopting a distance to OH 231.8 of 1 500 pc, translates into 4.1 km s$^{-1}$ per $10^{16}$ cm. From this value, a dynamical age for the molecular outflow of 770 yr is derived, a value which is also very similar to the one found for M 1–92 (900 yr) by Bujarrabal et al. (1998a). Since free movement is the easiest explanation for the remarkable constant velocity gradient found in OH 231.8, as well as in other PPNe, we interpret these Hubble-like velocity fields as the result of an interaction that took place at the beginning of the PPN phase, which lasted much less than the kinematical age of the accelerated gas. For the case of OH 231.8, we derive an upper limit to the duration of this post-AGB interaction of ∼125 yr.

The structure of the molecular envelope detected in CO can be divided in at least two components: the high velocity bipolar jet and the central core. For the high velocity bipolar CO jet, which corresponds to deprojected expansion velocities larger than ∼75 (i.e., LSR velocities outside the −10:+78 km s$^{-1}$ range), it is clear that its two components (the blueshifted one in the north and the redshifted one in the south) are not symmetric. The red CO jet in the south runs almost twice faster than the blue one in the north. Correspondingly, the southern CO jet is much larger that the one in the north, since they share the same velocity gradient (see above): 40″ against 17″. Another difference between the two jets is that the northern one ends abruptly – there is a clear cut –, while the one in the south shows a gradual weakening of its emission, which makes more difficult to establish its total extent (since it could depend on the sensitivity of the observations). In addition, the redshifted (southern) jet presents a sort of curling around the symmetry axis, with deviations from it as large as 3″–4″, while the blue counterpart strictly lies along the nebular axis of symmetry. Also, the jet in the north shows a continuous flow of matter, with a strong condensation at the end, while it is possible to find several breaks and condensations in the $^{12}$CO emission along the south tail.

Another outstanding feature shown by the interferometric observations, is the high collimation of the CO bipolar outflow. In the $J = 2-1$ line, the typical size of the CO outflow in the direction perpendicular to the axis (the deconvolved FWHP of the individual channel maps) ranges between 2.″0 and 3.″5. Given those widths, and defining the collimation factor as the ratio between the length and the width of the outflow, we find values for this collimation of ∼9 in the north and of ∼20 in the south (we have also corrected for the inclination of the axis with respect to the plane of the sky). These values are quite large, even in comparison with those of bipolar molecular outflows from young stellar objects. For the PPN M 1–92 the collimation factor of the molecular flow is much lower, but values of about 10–12 are found for the compact jet detected in atomic lines in the optical (see Bujarrabal et al. 1998a and 1998b).

The central core is a structure about 12″ long, centered at the star position, and corresponding to the emission detected between −40 and +110 km s$^{-1}$ (deprojected LSR velocities). Although the situation here is not so clear (because of the poorer spatial resolution in the north-south direction), based on observational similarities with the case of M 1–92, we suggest that the central core of OH 231.8 has a structure similar to that in M 1–92 (Bujarrabal et al. 1998a). Therefore, also for OH 231.8 we would have a central equatorial disk (or torus) perpendicular to the symmetry axis, and two hollow shells at both sides of this central disk; the two high velocity features also found in M 1–92 would correspond here to the much more prominent highly collimated bipolar flow discussed before. In the $^{12}$CO $J = 2-1$ maps, there is clear evidence for the presence of the proposed central structure at velocity channels +60.0 and +53.5 km s$^{-1}$ in the south lobe, and +7.9 and +1.4 km s$^{-1}$ in the north lobe. These maps, see Fig. 7, show ring/horseshoe-like emitting regions, elongated along the direction of the axis of symmetry, plus a strong condensation at the central star position. As for the case of M 1–92 the ring/horseshoe-like elongated feature would correspond to the two hollow shells, while the central condensation would be due to the presence of the thick equatorial disk. This structure, an equatorial disk dividing the two hollow lobes, is also clearly identified in our interferometric observations of SO (Paper II), that only probe the densest parts of the nebula.

As for the case of M 1–92, the shape of these hollow lobes suggests that they have been formed by means of bow shocks mostly advancing in the axial direction. Note that the high velocities found in the lobes are much larger than the expansion velocity measured at the equatorial disk detected in SO, about 8 km s$^{-1}$ (see Paper II), that probably corresponds to the expansion velocity of the original AGB envelope previous to any post-AGB acceleration. (We are therefore implicity assuming that the equatorial disk is those parts of the former AGB envelope not yet affected by the post-AGB acceleration.) This result also suggests that the hollow lobes have been formed by the passage of a shock.

The elongation of these ring/horseshoe-like structures tracing the hollow lobes can be used to estimate $i$, the angle of inclination of the symmetry axis with respect to the plane of the sky. For this purpose, we will assume that the velocity field of the nebula is essentially described by a radial expansion, with a speed proportional to the distance to the center. In this case, each channel map represents a cut of the nebula through a plane parallel to the plane of the sky (the different channels representing cuts at different deepness along the line of sight). Assuming that the nebula, and in particular the hollow shells of the two lobes are symmetric around the nebular axis, the relationship $\oslash_{\rm Maj} \sin(i) = \oslash_{\rm min}$ should hold; where $\oslash_{\rm Maj}$ and $\oslash_{\rm min}$ are, respectively, the major and minor diameter of the elliptical rings. In the south lobe the size of the ring/horseshoe, measured as the separation between the two opposite rims, is $\sim 4.''0 \times 2.''5$, whereas on the north is

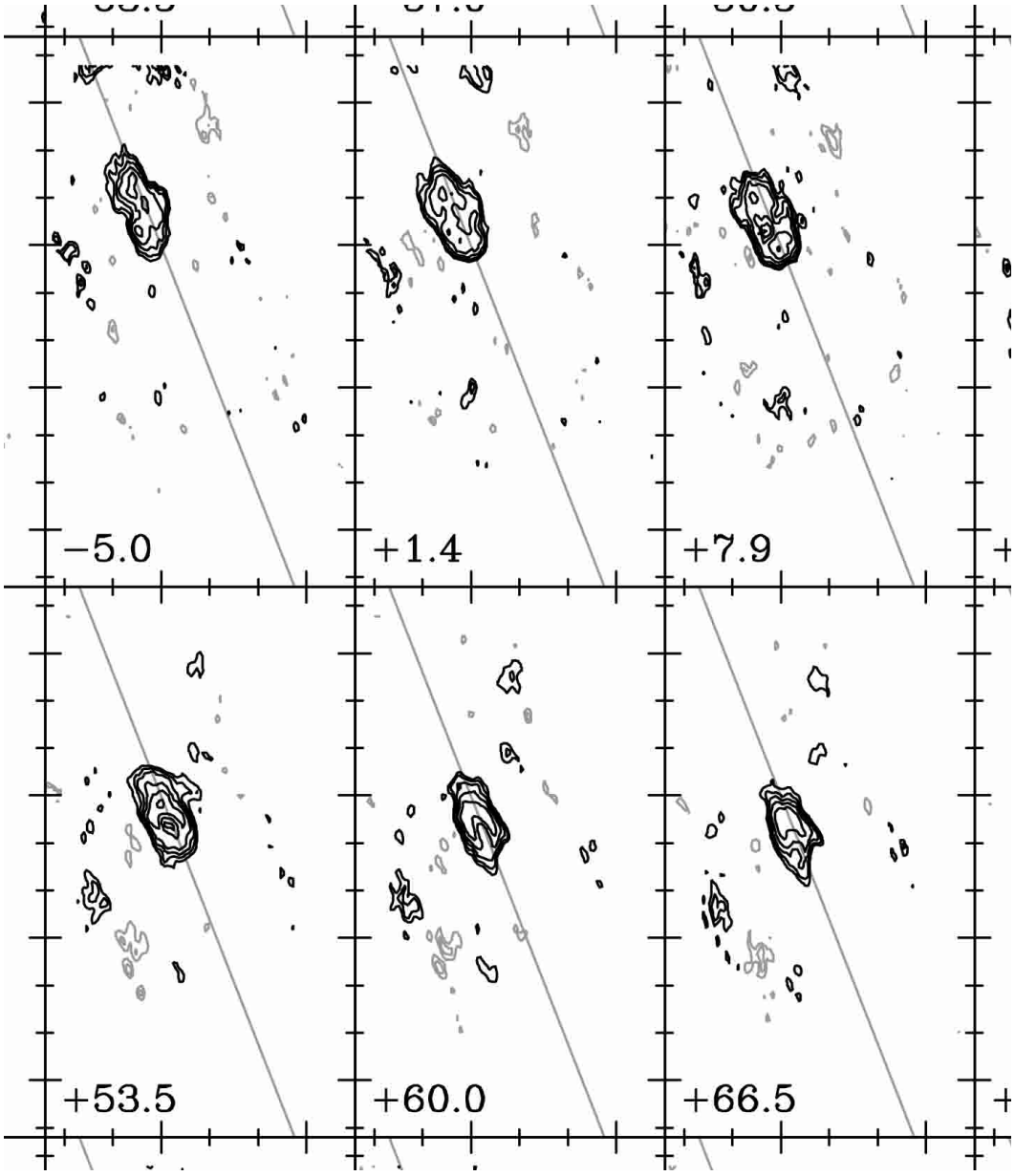


**Fig. 7.** A blow up of Fig. 3 better showing those channel maps for which a local minimum is detected at the center of the emission. These maps spatially correspond to the two lobes of the reflecting nebula. The ring/horseshoe-like shape of the $^{12}$CO $J = 2-1$ emission clearly indicates that the molecular gas lies mostly on the walls of the lobes, which are emptied. See Sect. 3.2 for more details.

$\sim 5\farcs5 \times 3\farcs0$. Threfore, from our observations we derive a value of $i$ of $\sim 35°$, in excellent agreement with the previously assumed value for this parameter, which has been derived in a completely independent way (see Sect. 1). On the other hand, this agreement indicates that the velocity field (and cylindrical symmetry) assumed must be a good approximation to the real case.

### 3.2.1. Comparison with the NIR data

As we have previously said (see Sect. 3.1), the main difference between the NIR and CO molecular emission maps is the absence of CO in the low level spherical component detected in the NIR images. We have also argued, in view of its radial intensity profile, that this component represents the remnant of the AGB mass loss occurred more than 4500 yr ago. If this is the case, the easiest explanation for the absence of CO in this part of the circumstellar envelope would be its photodissociation by the interstellar UV field. Under this assumption, we can use the non-detection of CO to estimate an upper limit to the amount of mass loss responsible for this component (otherwise very difficult to estimate since the NIR emission is probably due to second or higher order scattered photons). Using the results of Mamon et al. (1988), for CO to be photodissociated at radii larger than $10^{17}$ cm ($5''$ at a distance of 1500 pc) the mass loss should have been less than $2 \times 10^{-6}\ M_\odot\,\mathrm{yr}^{-1}$. Note that we are implicitly assuming

that the expansion velocity has not changed in the past. However, even if this is not the case, the results would not change very much; for an expansion velocity of 30 $\mathrm{km\,s^{-1}}$ Mamon et al. quote a mass loss rate of $5\times10^{-6}\ M_\odot\,\mathrm{yr^{-1}}$ for a similar photodissociation radius.

We can also learn about the mass loss history of OH 231.8 during the late AGB-phase by comparing the mass loss we have just estimated, with the value derived from the CO detected in the central core, which is still flowing at the AGB expansion velocity. The total mass of this central core is $\sim$0.64 $M_\odot$ (see next section and Table 2), and we have already estimated that this epoch of higher mass loss started $\sim$4000 yr ago, therefore we derive a huge average mass loss of $1.6\times10^{-4}\ M_\odot\,\mathrm{yr^{-1}}$. This result is not surprising if we consider that the present mass loss rate can not have lasted for much more than the time we have estimated; otherwise it would have exhausted the whole star (a 3 $M_\odot$ initial mass star can only support a mass loss of $1.6\times10^{-4}\ M_\odot\,\mathrm{yr^{-1}}$ for $\sim$10 000 yr). Although these calculations are very crude, they tell us that the mass loss in OH 231.8 should have substantially increased, at least by a factor 50 to 100, in the recent past (several thousand years ago). Note that this change in the mass loss rate is compatible with the order of magnitude of the increase in the scattered light intensity shown in Fig. 6. We are not claiming that 4500 yr ago the mass suddenly increased from $2\times10^{-6}\ M_\odot\,\mathrm{yr^{-1}}$ to $1.6\times10^{-4}\ M_\odot\,\mathrm{yr^{-1}}$, but that the mass loss rate has substantially increased (by a factor $\sim$100), during the last 4500 yr. Whether this increase was sudden or not we can not conclude from our simple analysis.

On the other hand, the presence of an efficient CO photodissociation in the spherical nebular component, raises the question of whether CO can survive in the bipolar outflow, specially at the far end of the south lobe, where we have detected CO at distances of at least $4.5\times10^{17}$ cm. Following van Dishoeck & Black (1988), the characteristic time for the CO photodissociation is about 150 yr, if we assume a standard interstellar UV flux. However, following the calculations by these authors and taking into account the shielding by dust grains and molecular hydrogen, as well as the self-shielding due to CO, for the column densities we derive from our maps and the $^{13}$CO single-dish data (see next section), this characteristic time is enlarged by a factor $\sim$20 to 50. Therefore we should expect CO to survive in the end of the south tail for $\sim$3000 to 5000 yr. Note that in this case we are dealing with molecular gas that has been exposed to the interstellar UV field in its present circumstances, only during a few hundred years at most. (On the contrary, the gas photodissociated in the spherical halo has been exposed to the UV field for more than 4500 yr.) Of course for inner regions in the molecular flow one should expect larger lifetimes for CO, since dust opacities and molecular column densities are also larger. We therefore conclude that the detection of relatively abundant CO in the bipolar outflow of OH 231.8 is fully compatible with our current understanding of CO/molecular photodissociation.

## 4. Physical parameters of the molecular envelope of OH 231.8+4.2

From our maps of the CO $J=1{-}0$ and $J=2{-}1$ lines, it is possible to estimate the rotational temperature, $T_\mathrm{r}$, of the emitting gas. This parameter should describe the excitation of the CO rotational ladder, assuming that the excitation temperatures are equal for all the rotational lines, or at least for the low-$J$ levels that are significantly populated. As it has been discussed by Bujarrabal et al. (1997) and Sánchez Contreras et al. (1997), such an assumption is reasonable for the conditions expected in OH 231.8 and similar objects, since the rotational transitions of CO show low Einstein coefficients and thus are easily thermalized. Precisely because of the easy thermalization of the low rotational lines of CO in the relevant cases, this rotational temperature is a good measure of the kinetic temperature of the emitting (molecular) gas.

To estimate $T_\mathrm{r}$, we will use the maximum brightness temperatures $T_\mathrm{B}$ at different distances along the symmetry axis of the nebula (following the wiggling of the CO emission on the south tail to probe all the molecular clumps). As input parameters for this computation we have taken the values for $^{21}T_\mathrm{B}$, and the ratio between $^{21}T_\mathrm{B}$ and $^{10}T_\mathrm{B}$. To minimize the possible effects of the different beam resolution, for the $T_\mathrm{B}$ ratio we have adopted $^{21}T_\mathrm{B}$ values after restoring the $J=2{-}1$ map with the clean beam of the $J=1{-}0$ line. (We are thus implicitly assuming that the brightness distributions of both lines are similar.) We have also multiplied the $^{21}T_\mathrm{B}$ values by a factor 1.5 in order to correct for the lost-flux/calibration problem in the interferometric maps of this line (see the previous discussion in Sect. 2.2). The relations between the $J=2{-}1$ and $J=1{-}0$ opacities and the source functions are well known, and only depend on $T_\mathrm{r}$, when this parameter can be defined. Therefore, from the values of $^{21}T_\mathrm{B}$ and $^{10}T_\mathrm{B}$ it is possible to determine $T_\mathrm{r}$ and both opacities, $^{21}\tau$ and $^{10}\tau$. Note that in this case $^{21}\tau$ and $^{10}\tau$ represent the opacities of the lines at maximum intensity, both in velocity and position perpendicular to the symmetry axis (i.e. for a given distance along this axis). The calculation of these parameters from the observational data is straightforward, only requiring a simple iterative code of fast convergence (at least in our case). This simple code, however, fails in calculating the line opacities when these are large ($\geq$ 3–5), but $T_\mathrm{r}$ should be reasonably well estimated even in this case.

Our results show that the CO lines are optically thick between $16''$ to the south and $6''$ to the north of the central star; this region essentially is coincident with the two bright lobes seen in the NIR images. The rotational temperature in the southern nebula, from $-37''$ up to $-10''$, ranges between 8 and 10 K. $T_\mathrm{r}$ increases toward the central star position, reaching a maximum value of $\sim$35 K, and decreasing again down to 15 K at $+5''$. In the north end of the nebula, there is a secondary maximum of $T_\mathrm{r}$, of 23 K, at $+12''$, in coincidence with the intensity maximum detected in both CO and NIR in the north lobe. This $T_\mathrm{r}$

increase further supports the existence of a strong shock interaction in this region, as it has been revealed by the optical spectroscopy of forbidden atomic lines (Paper I). These temperatures agree very well with the results obtained by Menten & Alcolea (1995) from their observations of the $(J,K) = (1,1)$ to (5,5) inversion transitions of ammonia. These authors also found a low kinetic temperature of $\sim$19 K for the velocity range +40: +80 km s$^{-1}$, and a higher one, $\sim$50 K, for the central line core.

Using these rotational temperatures and assuming that they also apply to the $^{13}$CO lines, we have improved our estimations for the mass, momentum and kinetic energy in the nebula based on our previous single-dish observations of the $^{12}$CO and $^{13}$CO $J = 1{-}0$ and $J = 2{-}1$ lines (see Sánchez Contreras et al. 1997). Note that the $^{13}$CO lines are optically thin and therefore allow a reliable determination of the mass. For such a purpose, we have done maps of $^{12}$CO integrated intensity for the velocity intervals considered in that paper (see Tables 2 and 1 in Sánchez Contreras et al. 1997). From these maps we have determined the spatial extent of the emission at each velocity range, and the corresponding characteristic rotational temperature, $T_{\rm r}$. These temperatures have been used to recompute the total amount of mass in the nebula per velocity interval from the $^{13}$CO intensities. These new results are presented in Table 2. Note that we have divided the velocity interval I6 in Sánchez Contreras et al. (1997), in two different intervals, since, as it is clear in the total integrated intensity maps, there are two distinct clumps detected at these velocities (see Fig. 4b). In this case, to determine the masses of the two clumps separately, we have assumed that the individual masses are proportional to the respective integrated intensity in the interferometric maps. The conversion factor, between the interferometric integrated $^{12}$CO $J = 2{-}1$ intensity and the total mass, determined in this way has been used to estimate also the mass of I7, a new velocity interval not considered in the single dish observations. Note that we can do this because for the velocity intervals I6a, I6b and I7, we have measured the same rotational temperature, and the opacities of the $^{12}$CO lines are low. In Table 2, we have added two extra lines summarizing the some global parameters of the north and south molecular flows (always excluding the central clump I3).

After correcting for the new $T_{\rm r}$ values, the main results obtained by Sánchez Contreras et al. (1997) still holds. The north lobe is slightly more massive and shows more momentum than the south one, which on the other hand is slightly more energetic. In any case, these differences are really minor, $\leq$15%, and it is not clear if they are related with the strong asymmetry found in extent, shape, and final velocity of the two directions of the flow.

Additionally, we have estimated the mean densities for the regions emitting in the velocity intervals previously considered. We simply divided the total mass by the volume of the corresponding emitting region at half power contour, assuming that the size along the line of sight is similar to that in the direction perpendicular to the symmetry axis of the nebula (i.e., we are assuming cylindrical symmetry along this axis). These densities are also shown in Table 2. Apart from the central core, where a value of $3.3 \times 10^6$ cm$^{-3}$ has been obtained, the mean densities in OH 231.8 do not vary very much. Except for the very distant I7 clump, densities vary less than an order of magnitude along the molecular flow: between $2.1 \times 10^4$ and $1.8 \times 10^5$ cm$^{-3}$. In the south lobe, the mean density decreases with the distance, roughly following a $1/r$ low (excluding I7). In the north lobe, on the contrary, the ending component, I1, is somewhat denser than the intermediate one, I2. This result also supports the idea that I1 represents a region with a currently active shock interaction (see Paper I).

## 5. Conclusions: the nature of OH 231.8+4.2 and its bipolar outflow

We have performed high-resolution interferometric observations of the $^{12}$CO $J = 1{-}0$ and $J = 2{-}1$ lines in the protoplanetary nebulae OH 231.8+4.2. High-quality NIR continuum images of scattered light were also obtained. Our observations probe the bulk of the nebular material, showing with a resolution $\sim$1″ the mass density distribution. The density in the CO outflow is found to be unexpectedly high, between $3.3 \times 10^6$ and $4 \times 10^3$ cm$^{-3}$, and systematically decreasing from the center to the southern edge. A relative condensation is found in the northernmost clump, that is probably associated to a strong bow-like shock. Since velocities are also measured in CO, the dynamic parameters (kinetic momentum and energy) are also mapped with the same spatial resolution. Finally, the combination of both $^{12}$CO $J = 1{-}0$ and $J = 2{-}1$ lines has been used to measure the distribution of the kinetic temperature in the nebula, which is found to be very low, ranging between 8 K, in the outer southern clumps, and, in the central region, 35 K; again a relative temperature increase is found in the northern condensation.

Most of the nebular mass ($\sim$0.64 $M_\odot$) is located in the central condensation and flows at expansion velocities $\leq$40 km s$^{-1}$. The rest of the molecular gas, about 0.3 $M_\odot$ almost equally distributed along the two directions of the symmetry axis of the nebula, flows at high expansion velocities. We find that these axial velocities increase proportionally to the distance to the central star, reaching values as large as 430 km s$^{-1}$. The general mass distribution in OH 231.8+4.2 is found to be very elongated, with a length/width ratio of 20 in the southern tail. Most of the nebular extension is composed of a very elongated and clumpy structure. In the center, however, we find a double hollow-lobe structure, similar to those found in the well studied nebulae M 1–92 (Bujarrabal et al. 1998a) and M 2–56 (unpublished Plateau de Bure maps) but somewhat less extended. Assuming free expansion, the hollow shells in OH 231.8+4.2 will develop into a structure similar to that of M 1–92 in a few hundred years.

One of the most remarkable features of the bipolar molecular outflow in OH 231.8 is its enormous kinetic

**Table 2.** Physical properties of the different clumps identified from our CO data.

| | LSR vel. range ($\mathrm{km\,s^{-1}}$) | $T_\mathrm{r}$ (K) | Mass ($M_\odot$) | Dens. ($\mathrm{cm^{-3}}$) | Dist. ($''$) | $V_i$ ($\mathrm{km\,s^{-1}}$) | Momentum ($M_\odot$ $\mathrm{km\,s^{-1}}$) | $E_\mathrm{kin}$ ($M_\odot$ $\mathrm{km^2\ s^{-4}}$) |
|---|---|---|---|---|---|---|---|---|
| I1 | −80: −30 | 23 | 0.05 | $1.8\times10^5$ | +12 | 150 | 7.5 | 563 |
| I2 | −30: 10 | 15 | 0.1 | $1.3\times10^5$ | +5 | 73 | 7.3 | 266 |
| I3 | 10: 55 | 35 | 0.64 | $3.3\times10^6$ | 0 | | | |
| I4 | 55: 80 | 25 | 0.1 | $1.3\times10^5$ | −5 | 59 | 5.9 | 174 |
| I5 | 80: 150 | 10 | 0.027 | $8.5\times10^4$ | −10 | 140 | 3.8 | 266 |
| I6a | 150: 205 | 8 | 0.006 | $3.0\times10^4$ | −20 | 246 | 1.5 | 185 |
| I6b | 205: 230 | 8 | 0.003 | $2.1\times10^4$ | −27 | 314 | 0.9 | 148 |
| I7 | 230: 285 | 8 | 0.001 | $4.0\times10^3$ | −37 | 421 | 0.4 | 84 |
| North | | | 0.15 | | | | 14.8 | 829 |
| South | | | 0.14 | | | | 12.5 | 857 |

linear momentum, a common property of the high velocity molecular emission in post-AGB sources (Bujarrabal et al. 1998a, 2001a). In the case of OH 231.8, the linear momentum carried by the envelope is about 27 $M_\odot\,\mathrm{km\,s^{-1}}$ ($5.5\times10^{39}$ $\mathrm{g\,cm\,s^{-1}}$); note that this total parameter is not exactly a linear momentum but a scalar linear momentum obtained from spatial integration of the momentum moduli. The kinetic energy carried by the bipolar outflow is also very high, ∼1700 $M_\odot\,\mathrm{km^2\,s^{-4}}$ (∼$3.4\times10^{46}$ erg). It is remarkable that the scalar momentum carried per unit time by the stellar radiation in this source is only ∼$4\times10^{34}$ $\mathrm{g\,cm\,s^{-1}\,yr^{-1}}$ (Bujarrabal et al. 2001a). So the stellar radiation would have needed more than $10^5$ yr to release such a large linear momentum. We have however argued that the whole life of the nebula (in its present kinematics) is ∼770 yr, and that the gas acceleration probably took place in just a small fraction of this time. The measured momentum of the molecular bipolar outflow is then larger than that carried by the stellar photons, during the gas acceleration time, by a factor ∼1000, for the present luminosity of the source.

It is well known that during the AGB phase, stars loose mass due to the photon pressure of the stellar light acting onto the circumstellar grains, which transfer the gained momentum to the circumstellar gas thanks to the existence of drag forces, originated in the gas-dust collisions due to the different expansion velocities for the gaseous and solid phases of the envelope (the dust moves faster than the gas). The linear momentum transferred to the gas per unit of time is given by the following expression (for details see Bujarrabal et al. 2001a, 2001b):

$$P \sim Q\tau_\mathrm{eff} t_\mathrm{acc} L/c. \quad (1)$$

In this equation, $t_\mathrm{acc}$ is the time during which the gas acceleration took place. $Q$ is the photon pressure efficiency, which depends of both stellar temperature and circumstellar grain properties. $Q \leq 1$ if stellar photons are simply absorbed by the envelope, and ∼2 if all photons suffer just backward scattering; we will assume that $Q \sim 1$. $\tau_\mathrm{eff}$ is the opacity in the wavelengths at which the star+envelope emits, i.e. the optical or NIR when the envelope is optically thin and the range 5–20 $\mu$m when it is very thick. This factor is introduced to account for the possible multiple absorption/scattering of a photon before it leaves the envelope. In thick nebulae, like OH 231.8, the opacity must be computed in the IR because, since the efficiency of the pure absorption and the scattering are not very different, it is difficult to have many scattering events before a photon is absorbed by a grain. Once a stellar photon is absorbed, it can be reemitted but in the infrared, where the opacity is much lower and yet the efficiency of the scattering drops drastically. In very opaque nebulae, like OH 231.8, this equivalent opacity could raise a value up to 5–10, but not much more than that (Bujarrabal et al. 2001b). Note that we are assuming photon pressure acting directly on the dust grains. The case of photon pressure acting directly on optically thick ionized gas around hot stars is completely different; here much larger values of $Q\tau_\mathrm{eff}$ can be easily attained. However, for a normal AGB or young PPN, the photon pressure on the gas phase is much more inefficient than that onto grains. Therefore, even if we take a value of $\tau_\mathrm{eff}$ of about 10, and we allow the photon pressure to work for the whole life of the bipolar flow, we still have a kinetic momentum excess by a factor ∼20.

One may think that the present luminosity of the source was much large in the past (something really difficult to support). However, this would not make photon pressure to work in this particular case because of an additional constrain set by the drag force. It can be shown that, for expansion velocities larger than the sound speed and gas to dust mass ratios much larger than 1 (as it is the case here), the difference in velocity between the dust and the gas is given by the expression:

$$v_\mathrm{drag} \equiv v_\mathrm{dust} - v_\mathrm{gas} \approx \sqrt{\frac{\tau_\mathrm{eff} L_\star v_\mathrm{gas}}{\dot{M}\ c}} = v_\mathrm{gas}\sqrt{\frac{\tau_\mathrm{eff} L_\star/c}{P}} \quad (2)$$

(provided that $\tau_\mathrm{eff}$ is larger than 1; see e.g. Goldreich & Scoville 1976 and Habing et al. 1994). In this formula, $v_\mathrm{dust}$ and $v_\mathrm{gas}$ are respectively the dust and gas expansion velocities.

For the value of $L_*$ needed to explain the high momentum measured from CO, we derive drag velocities larger than 100 $\mathrm{km\,s^{-1}}$ to push the molecular gas up to the observed velocities; i.e. we need to have dust moving significantly faster than the gas. However, we have seen in

the comparison of the NIR and CO images that both components, gas (probed by CO) and dust (probed by NIR scattering images), present structures along the axis that spatially match each other better than 5% for the southern clumps (both maps agree better than 1″ even for structures located more than 20″ away from the center). Therefore none of the two nebular components can have significantly large velocities than the other. On the contrary, the similar appearance of both circumstellar phases clearly indicates that whatever pushed the envelope along the axis, it ejected a force either directly on both gas and dust, or just on the gas, but not just on the dust. (It can be shown that if the gas is directly pushed, since it is the most massive component, it would drag the dust without a significant velocity difference.) A similar reasoning can be applied to the only other PPN that has been mapped in CO and scattered light with accuracy enough, M 1–92, in which both images are coincident and the momentum also exceeds that provided by the stellar radiation (Bujarrabal et al. 1998a, 1998b).

One further argument against photon pressure as responsible for the observed bipolar outflow is the large expansion velocities found, exceeding 100 km s$^{-1}$. These velocities are much larger than those typically observed in AGB circumstellar envelopes (AGB-CEs), for which expansion velocities in excess of 40 km s$^{-1}$ are very rare, and always associated to high-luminosity sources, i.e. supergiants (te Lintel Hekkert et al. 1991; Habing et al. 1994). Following Habing et al. (1994), for a high mass loss rate as it is the case of OH 231.8+4.2, the final expansion velocity in a CE, $v_\infty$, depends very little on parameters like the mass loss rate and grain size $a$. According to these authors, for $\dot{M}$ larger than $10^{-5}\ M_\odot\,\mathrm{yr}^{-1}$, $v_\infty \propto L_\star^{0.3}\delta^{0.5}(\dot{M}/a)^{0.04}$, where $\delta$ is the gas-to-dust mass ratio (typically 0.01 for O-rich sources). Therefore, in order to attain $v_\infty$ of the order of 200 km s$^{-1}$, we should assume a luminosity ∼200 times that of a supergiant, or a gas-to-dust ratio of the order of 1 for $L_\star \sim 10^4\ L_\odot$, these two possibilities being extremely unlikely.

We must therefore conclude that the standard mechanism powering the mass loss process in AGB envelopes, i.e. radiation pressure acting onto grains, cannot explain the acceleration of the bipolar flow in OH 231.8+4.2. Our data do not show what this mechanism could be (for speculations on this topic see Bujarrabal et al. 2001b), but definitely rule out photon pressure, acting like during the AGB phase. We suggest that this result should apply to most PPNe.

An apparent solution to the problem of the origin of the momentum would be that the molecular flow was accelerated by a shock propagating in the axial direction. In this case, post-AGB very collimated jets would impinge onto the dense AGB shell, that would be accelerated by the subsequent shocks and become the presently observed fast molecular flows. Such a scenario is suggested by the shape of the inner hollow shells and by the presence of optical lines from shock-excited gas. However, this thesis just postpones the problem to the explanation of the origin of the enormous momentum that the post-AGB jets would have to carry (see further discussion in Bujarrabal et al. 2001b).

### 5.1. The nature and evolutionary status of OH 231.8+4.2

An important clue for determining the evolutionary status of OH 231.8 is given by its very probable association with the open cluster NGC 2437 (M 46). This association is supported by their coincidence in distance and radial velocity. For the cluster, a weighted mean LSR velocity of 23 km s$^{-1}$ ($V_{\mathrm{HEL}}$ 41 km s$^{-1}$) has been computed, with a dispersion of 5 km s$^{-1}$ (Cuffey 1941). Therefore, the LSR systemic velocity of OH 231.8 of ∼34 km s$^{-1}$ is fully compatible with its belonging to the cluster. The distance to NGC 2437 has been estimated to be between 1400 and 1600 pc (see Lyngå 1987, and references therein), in excellent agreement with the value determined for OH 231.8 of 1500 pc. Note that none of these distances are determined kinematically, and therefore this coincidence is independent on the similar velocities of the two objects. For the cluster, an age of $3 \times 10^8$ yr has also been derived (Mermilliod 1981), and therefore a similar age can be assumed for OH 231.8. This short age for an AGB star strongly suggest that we are dealing with a very massive object, with a main-sequence progenitor of ∼3 $M_\odot$, according to Jura & Morris (1985). This high mass scenario agrees, on the other hand, with other characteristics of the source determined here, like the extremely high mass loss rate, the very massive envelope, and the large amount of energy involved in the PPN kinematics.

As we have said before, it has been suggested that there might be a double star at the center of OH 231.8, based on the detection of a weak blue excess in the stellar continuum scattered at the reflecting lobes (Cohen et al. 1985). This scenario is very appealing, since one of the most widely accepted mechanisms for producing bipolar collimated outflows during the post-AGB evolution would be the presence of a binary system, thanks to the accretion of the mass lost by the primary onto the secondary (e.g. Soker & Rappaport 2000). Note however, that the double system hypothesis is not the only possible explanation for the presence of such a blue excess (e.g. an anomalous photospheric structure due to the existence of hot spots). In fact there are strong arguments against that interpretation. If there is a blue companion to the red giant, QX Pup would be a symbiotic system. These systems are indeed known to power fast and highly collimated bipolar ejections (see the case of R Aqr, Hollis et al. 1999), however, the characteristic of the molecular envelope of OH 231.8 would be rather unique for a symbiotic star. Although many symbiotics show infrared excess due to presence of circumstellar grains, OH 231.8 would be the first symbiotic system with a thick molecular envelope; so far, no other system has been detected in CO. In fact, there are only two cases for which the existence of circumstellar

molecular gas has been proved by the detection of SiO maser lines: R Aqr and H 1–36 (in spite of the existing deep surveys, see e.g. Schwarz et al. 1995). Note that OH 231.8 is also detected in SiO maser emission. Moreover, there is no direct evidence for a companion, even in the recent high resolution images provided by the HST-NICMOS2 camera (Bieging et al. 2000). Therefore we should conclude that either OH 231.8 is a very peculiar symbiotic, or that observations are in contradiction with assuming the presence of a companion to the QX Pup red giant.

On the other hand, there is material very close to the Mira component, as it is evidenced by the presence of relative strong SiO masers (e.g. Paper II). SiO masers are always located in the vicinity of the stars, at several $10^{14}$ cm, because their pumping mechanism (regardless whether is due to collisions or to the stellar 8 $\mu$m radiation) require a strong source of energy. Indeed, the existing mapping is compatible with such a compact distribution (Paper II). Also, these SiO emission tell us that the circumstellar density in the vicinity of the star is relatively high ($10^9$–$10^{10}$ cm$^{-3}$). Therefore we should conclude that the copious mass loss typical of the latest phases of the AGB is still going on, or has ceased just a few years ago.

One interesting possibility of reconciling the post-AGB nature of the envelope and the apparently AGB status of the central source, would be that this latter has undergone a "born-again" evolution. In this scenario, the last thermal pulse occurs after the star lefts the AGB. The helium flash forces the source to move back to a red giant status, starting its blueward evolution again but now being a helium burning star; these scenarios have been proposed for explaining anomalous abundances in post-AGB stars (see e.g., Blöcker & Schönberner 1997, and references therein). In particular, if the last helium flash happens soon after the end of the AGB, the time necessary to complete the loop, returning to the AGB, can be very short. Blöcker & Schönberner (1997) have made detailed computations for this type of evolution for different initial masses. They found that if the initial mass of the source is $\sim$3 $M_\odot$, the time necessary to return to the AGB is only 290 yr, for a model in which the star undergoes its last thermal pulse 3200 yr after it left the AGB. These time-scales could fit to our case. According to that calculation, by the time the molecular envelope was strongly accelerated, 770 yr ago, QX Pup would have been much hotter, i.e., a normal post-AGB source. Later on the helium flash would have move the star back to the AGB, while the envelope remained expanding. Though this scenario seems very attractive, it is rather speculative: as far as we know, no other evidence that QX Pup has gone this type of "born again" evolution has been found.

Finally, we note that, although the bipolar nebula of OH 231.8 is characteristic of PPNe, it shows an important property that has not been observed in others: the two very elongated lobes. We have mentioned that the inner, hollow shells of OH 231.8 are expected to evolve, becoming very similar to the lobes found in M 1–92 and M 2–56 in less than 1000 yr. However, these nebulae do not present these long tails, and we have argued that the CO molecules detected in the southern clumps of OH 231.8 are not expected to be photodissociated in such a short time.

Our present knowledge on this remarkable object does not yet allow to depict a conclusion on its nature and evolutionary status. We have shown that the OH 231.8 nebula is unique: no (other) AGB, post-AGB or symbiotic star is surrounded by an envelope with comparable characteristics. The inner hollow lobes in OH 231.8 are similar to those found in other PPNe except for being somewhat less evolved, but the very long and narrow tails, particularly the southern one, have no counterpart in other known PPNe and do not seem to be evolving to something comparable. (Moreover, its central AGB star is not expected for a PPNe.) On the other hand, the envelopes around AGB stars are spherical or at most show small departures from this symmetry (e.g. Neri et al. 1998). Finally, symbiotic stars are often surrounded by bipolar nebulae, but not at all comparable to the massive molecular one of OH 231.8. So, the question we discussed in the Introduction, is OH 231.8+4.2 exceptional because it is now in a very short (crucial) evolutionary stage or because it is a peculiar object following a peculiar evolution?, has not a reliable answer yet.

*Acknowledgements.* We acknowledge the IRAM staff from the Plateau de Bure and from Grenoble for carrying the observations and help provided during the data reduction. We also thank the referee, Dr. G. Mellema, for his helpful comments. This work has been financially supported by the Spanish DGES, under project PB96-0104.

## References

Alcolea, J., Bujarrabal, V., & Sánchez Contreras, C. 1996, A&A, 312, 560
Bieging, J. H., Meakin, C. A., Kelly, D. M., et al. 2000, in Asymmetrical Planetary Nebulae II: From Origins to Microstructures, ed. J. H. Kastner, N. Soker, & S. Rappaport, ASP Conf. Ser., 199, 183
Blöcker, T., & Schönberner 1997, A&A, 324, 991
Bowers, P. F., & Morris, M. 1984, ApJ, 276, 646
Bujarrabal, V., Alcolea, J., Neri, R., & Grewing, M. 1997, A&A, 320, 540
Bujarrabal, V., Alcolea, J., & Neri, R. 1998a, A&A, 504, 915
Bujarrabal, V., Alcolea, J., Sahai, R., Zamorano, J., & Zijltra, A. A. 1998b, A&A, 331, 361
Bujarrabal, V., Castro-Carrizo, A., Alcolea, J., & Sánchez Contreras, C. 2001a, A&A, submitted
Bujarrabal, V., Castro-Carrizo, A., Alcolea, J., & Sánchez Contreras, C. 2001b, A&A, submitted
Cohen, M., Dopita, M. A., Schwartz, R. D., & Tielens, A. G. G. M. 1985, ApJ, 297, 702C
Cuffey, J. 1941, ApJ, 94, 55
Goldreich, P., & Scoville, N. 1976, ApJ, 205, 144
Guilloteau, S., Delannoy, J., Downes, D., et al. 1992, A&A, 262, 624
Habing, H. J., Tignon, J., & Tielens, A. G. G. M. 1994, A&A, 286, 523
Hollis, J. M., Vogel, S. N., Van Buren, D., et al. 1999, ApJ, 522, 297

Jura, M., & Morris, M. 1985, ApJ, 292, 487
Kastner, J. H., & Weintraub, D. A. 1995, AJ, 109, 1211
Kastner, J. H., Weintraub, D. A., Zuckerman, B., et al. 1992, ApJ, 398, 552
Kastner, J. H., Weintraub, D. A., Merril, K. M., & Gatley, I. 1998, AJ, 116, 1412
Lyngå, G. 1987, Lund Catalogue of Open Cluster Data (5th Ed.), Lund Observatory
Mamon, G. A., Glassgold, A. E., & Huggins, P. J. 1988, ApJ, 328, 797
Menten, K. M., & Alcolea, J. 1995, ApJ, 448, 416
Mermilliod, J. C. 1981, A&A, 97, 235
Morris, M., Guilloteau, S., Lucas, R., & Omont, A. 1987, ApJ, 321, 888
Neri, R., Kahane, C., Lucas, R., Bujarrabal, V., & Loup, C. 1998, A&AS, 130, 1
Sánchez Contreras, C., Bujarrabal, V., & Alcolea, J. 1997, A&A, 327, 689
Sánchez Contreras, C., Bujarrabal, V., Miranda, L. F., & Fernández-Figueroa, M. J. 2000a, A&A, 355, 1103, Paper I
Sánchez Contreras, C., Bujarrabal, V., Neri, J., & Alcolea, J. 2000b, A&A, 357, 651, Paper II
Soker, N., & Rappaport, S. 2000, ApJ, 538, 241
Shure, M., Sellgren, K., Jones, T. J., & Klebe, D. 1995, AJ, 109, 721
Schwarz, H. E., Nyman, L.-Å., Seaquist, E. R., & Ivison, R. J. 1995, A&A, 303, 833
te Lintel Hekkert, P., Caswell, J. L., Habing, H. J., Haynes, R. F., & Norris, R. P. 1991, A&AS, 90, 327
Reipurth, B. 1987, Nature, 325, 787
van Dishoeck, E. F., & Black, J. H. 1988, ApJ, 334, 771